Jumping with Variably Scaled Discontinuous Kernels (VSDKs)

Preprint · August 2018

CITATIONS
0

READS
122

3 authors:

Stefano De Marchi
University of Padova
106 PUBLICATIONS **836** CITATIONS
SEE PROFILE

Francesco Marchetti
University of Padova
4 PUBLICATIONS **4** CITATIONS
SEE PROFILE

Emma Perracchione
University of Padova
27 PUBLICATIONS **145** CITATIONS
SEE PROFILE

Jumping with Variably Scaled Discontinuous Kernels (VSDK)

S. De Marchi* F. Marchetti† E. Perracchione‡
francesco.marchetti.1@phd.unipd.it; demarchi@math.unipd.it;
emma.perracchione@math.unipd.it

August 12, 2018

Keywords
Jump discontinuities, discontinuous kernels, Gibbs phenomenon, variably scaled kernels, deep learning for satellite images.

Abstract

In this paper we address the problem of approximating functions with discontinuities via kernel-based methods. The main result is the construction of discontinuous kernel-based basis functions. The linear spaces spanned by discontinuous kernels lead to a very flexible tool which sensibly reduces the well-known *Gibbs phenomenon* in reconstructing functions with jumps. For the new basis we provide error bounds and numerical results that support our claims. The method is also effectively tested for approximating satellite images.

1 Introduction

Radial Basis Function (RBF) methods (refer e.g. to [12, 13, 24, 26]) have become one of the most popular tools for solving multidimensional scattered data problems. Thanks to their independence from the mesh and to their easy implementation, they find applications in a wide varieties of fields, such as population dynamics, machine (deep) learning, solution of PDEs and image registration.

Even if such meshfree approaches have been extensively studied in the recent years, especially focusing on the efficiency and stability of the interpolant (cf. e.g. [4, 5, 10, 15]) not much effort has been addressed to construct robust approximants for functions with jumps. Indeed, infinitely smooth RBFs, such as Gaussians and Multiquadrics, theoretically show spectral accuracy, which is no longer preserved when interpolating functions with discontinuities. This fact, first observed in the context of truncated Fourier expansions and

*Dipartimento di Matematica "Tullio Levi-Civita", Università di Padova, Italy
†Dipartimento di Salute della Donna e del Bambino, Università di Padova, Italy
‡Dipartimento di Matematica "Tullio Levi-Civita", Università di Padova, Italy

later used to characterize non-physical oscillations in the approximation of discontinuous functions, is known as *Gibbs phenomenon*.

To mitigate this effect for kernel-based approximation one can use linear RBFs (see e.g. [14] for a general overview). This has been done in [18], where the Multiquadric has been replaced by the linear spline in regions around discontinuities. Alternatively, post-processing techniques, such as Gegenbauer reconstruction procedure [16] or digital total variation [23], are well-established tools. Finally, we point out that also the so-called Variably Scaled Kernels (VSKs) [1] are truly performing when reconstructing functions with gradient discontinuities, as proven in [22]. Further, VSKs for detecting jumps have also been experimentally used in [21]; see also [3].

Based on the last mentioned papers, here we investigate both computationally and theoretically their behaviour. The basis associated to the discontinuous RBFs, constructed by means of what we will call the Variably Scaled Discontinuous Kernels (VSDKs), enables us to naturally reconstruct jump discontinuities (even with the family of Gaussians). The only drawback of the procedure lies in the fact that the algorithm needs to know where the discontinuities occur. To address this computational issue, one can consider widely used schemes, such as *Canny* or *Sobel* edge detection (cf. [2, 25]).

After providing a theoretical analysis of the scheme for the one dimensional case, we extend the idea to higher dimensions and we provide very general error bounds in terms of the well-known *power function*. Extensive numerical experiments are devoted to show the effectiveness of the method. We also point out that we provide a MATLAB code, freely available for the scientific community at `www.math.unipd.it/~demarchi/RBF/RBFCAA.html`, that can be used to reproduce the tests and experiments presented in the paper. To conclude, we also present applications to the reconstruction of satellite images (see[19]).

The paper is organized as follows. In Section 2, we briefly review the main theoretical aspects of kernel-based approximation methods and introduce the VSKs. Section 3 presents our method for VSDKs and in Section 4 we show extensive numerical experiments. Applications to real world data are reported in Section 5. In the last section we conclude.

2 Kernel-based approximation methods

Let $\mathcal{X} = \{\boldsymbol{x}_i,\ i = 1, \dots, N\} \subset \Omega$ be a set of distinct data points (or data sites or nodes) arbitrarily distributed on a domain $\Omega \subseteq \mathbb{R}^d$ and let $\mathcal{F} = \{f_i = f(\boldsymbol{x}_i),\ i = 1, \dots, N\}$ be an associated set of data values (measurements or function values) obtained by sampling some (unknown) function $f : \Omega \longrightarrow \mathbb{R}$ at the nodes $\boldsymbol{x}_i$. We can reconstruct f by interpolation, that is by finding a function $\mathcal{R} : \Omega \longrightarrow \mathbb{R}$ satisfying the conditions

$$\mathcal{R}(\boldsymbol{x}_i) = f_i, \quad i = 1, \dots, N. \tag{1}$$

The interpolation problem (1) has unique solution if $\mathcal{R} \in \text{span}\{\Phi_\varepsilon(\cdot, \boldsymbol{x}_i), \boldsymbol{x}_i \in \mathcal{X}\}$, where $\Phi_\varepsilon : \Omega \times \Omega \longrightarrow \mathbb{R}$ is a strictly positive definite and symmetric kernel. R can also depend on a so-called *shape parameter* $\varepsilon > 0$. The resulting kernel-based interpolant, denoted by $\mathcal{R}_{\varepsilon,\mathcal{X}}$, can be written as

$$\mathcal{R}_{\varepsilon,\mathcal{X}}(\boldsymbol{x}) = \sum_{k=1}^{N} c_k \Phi_\varepsilon(\boldsymbol{x}, \boldsymbol{x}_k), \quad \boldsymbol{x} \in \Omega. \tag{2}$$

We can write (1) by using the matrix $A_\varepsilon \in \mathbb{R}^{N\times N}$ which has entries $(A_\varepsilon)_{ik} = \Phi_\varepsilon(\boldsymbol{x}_i, \boldsymbol{x}_k),\ i,k = 1,\dots,N$. Then, letting $\boldsymbol{f} = (f_1,\dots,f_N)^T$ the vector of data values, we can find the coefficients $\boldsymbol{c} = (c_1,\dots,c_N)^T$ by solving the linear system $A_\varepsilon \boldsymbol{c} = \boldsymbol{f}$. Since we consider strictly positive definite and symmetric kernels, the existence and uniqueness of the solution of the linear system is ensured.

More precisely, we are interested in the class of strictly positive definite and symmetric *radial kernels* Φ_ε so defined.

Definition 2.1 *Φ_ε is called radial kernel if there exists a continuous function $\varphi_\varepsilon : [0,+\infty) \longrightarrow \mathbb{R}$, depending on the shape parameter $\varepsilon > 0$, such that*

$$\Phi_\varepsilon(\boldsymbol{x},\boldsymbol{y}) = \varphi_\varepsilon(\|\boldsymbol{x}-\boldsymbol{y}\|_2), \tag{3}$$

for all $\boldsymbol{x},\boldsymbol{y} \in \Omega$.

From (3) it follows that if Φ_ε is radial, then it is completely identified by the function φ_ε and we can indifferently use Φ_ε or φ_ε for denoting the interpolant in (2).

To Φ_ε we associate a real pre-Hilbert space $H_{\Phi_\varepsilon}(\Omega)$ with reproducing kernel Φ_ε

$$H_{\Phi_\varepsilon}(\Omega) = \mathrm{span}\{\Phi_\varepsilon(\cdot,\boldsymbol{x}),\ \boldsymbol{x}\in\Omega\},$$

equipped with a bilinear form $(\cdot,\cdot)_{H_{\Phi_\varepsilon}(\Omega)}$. We then define the *native space* $\mathcal{N}_{\Phi_\varepsilon}(\Omega)$ of Φ_ε as the completion of $H_{\Phi_\varepsilon}(\Omega)$ with respect to the norm $||\cdot||_{H_{\Phi_\varepsilon}(\Omega)}$, that is $||f||_{H_{\Phi_\varepsilon}(\Omega)} = ||f||_{\mathcal{N}_{\Phi_\varepsilon}(\Omega)}$ for all $f \in H_{\Phi_\varepsilon}(\Omega)$ (for details see the mongraphs [13, 26]).

The accuracy of the interpolation process is usually expressed in terms of the *power function*. Let $A_\varepsilon(\mathcal{X})$ be the interpolation matrix related to the set of nodes $\mathcal{X}$ and the kernel Φ_ε. Also let $A_\varepsilon(\mathcal{Y})$ the matrix associated to the augmented set $\mathcal{Y} \coloneqq \{\boldsymbol{x}\}\cup\mathcal{X},\ \boldsymbol{x}\in\Omega$. The power function is the positive function (cf. [7, 11])

$$P_{\Phi_\varepsilon,\mathcal{X}}(\boldsymbol{x}) := \sqrt{\frac{\det(A_\varepsilon(\mathcal{Y}))}{\det(A_\varepsilon(\mathcal{X}))}}\,. \tag{4}$$

obtained by the ratio of two determinants.

The following result holds (see e.g. [13, Th. 14.2, p.117]).

Theorem 2.1 *Let $\Phi_\varepsilon \in C(\Omega\times\Omega)$ be a strictly positive definite kernel and that $\mathcal{X} = \{\boldsymbol{x}_i, i = 1,\dots,N\} \subseteq \Omega$ has distinct points. For all $f \in \mathcal{N}_{\Phi_\varepsilon}(\Omega)$*

$$|f(\boldsymbol{x}) - \mathcal{R}_{\varepsilon,\mathcal{X}}(\boldsymbol{x})| \le P_{\Phi_\varepsilon,\mathcal{X}}(\boldsymbol{x})||f||_{\mathcal{N}_{\Phi_\varepsilon}(\Omega)}, \quad \boldsymbol{x}\in\Omega.$$

Remark 2.1 *Theorem 2.1 bounds the error with respect to the power function that depends on the kernel and data but is independent of the function values.*

2.1 From RBF to VSK interpolation

As well-known, the choice of the shape parameter ε is a crucial computational issue in RBF interpolation which also lead to instability problems. To overcome such problems in [1] were introduced the so called VSKs and in [22] they have been used to reconstruct functions with gradient discontinuities.

We recall that in VSKs the tuning of the shape parameter is replaced by the choice of a *scale function*. More precisely a VSK is defined as follows. (cf. [1, Def. 2.1]).

Definition 2.2 *Letting $\mathcal{I} \subseteq (0, +\infty)$ and Φ_ε a positive definite radial kernel on $\Omega \times \mathcal{I}$ depending on the shape parameter $\varepsilon > 0$. Given a scale function $\psi : \Omega \longrightarrow \mathcal{I}$, we define a VSK Φ_ψ on Ω as*

$$\Phi_\psi(\boldsymbol{x}, \boldsymbol{y}) \coloneqq \Phi_1((\boldsymbol{x}, \psi(\boldsymbol{x})), (\boldsymbol{y}, \psi(\boldsymbol{y}))), \tag{5}$$

for $\boldsymbol{x}, \boldsymbol{y} \in \Omega$.

Defining the map $\Psi(\boldsymbol{x}) = (\boldsymbol{x}, \psi(\boldsymbol{x}))$ on Ω, the interpolant on the set of nodes $\Psi(\mathcal{X}) \coloneqq \{(\boldsymbol{x}_k, \psi(\boldsymbol{x}_k)),\ \boldsymbol{x}_k \in \mathcal{X}\}$ with fixed shape parameter $\varepsilon = 1$ takes the form

$$\mathcal{R}_{1,\Psi(\mathcal{X})}(\Psi(\boldsymbol{x})) = \sum_{k=1}^{N} c_k \Phi_1(\Psi(\boldsymbol{x}), \Psi(\boldsymbol{x}_k)), \tag{6}$$

with $\boldsymbol{x} \in \Omega,\ \boldsymbol{x}_k \in \mathcal{X}$.

By analogy with the interpolant in (2), the vector of coefficients $\boldsymbol{c} = (c_1, \ldots, c_N)^T$ in (6) is determined by solving the linear system $A_\psi \boldsymbol{c} = \boldsymbol{f}$, where $(A_\psi)_{ik} = \Phi_\psi(\boldsymbol{x}_i, \boldsymbol{x}_k)$ and $\boldsymbol{f}$ is the vector of data values. We point out that the considered linear system has a unique solution since Φ_ψ is strictly positive definite.

Once we have the interpolant $\mathcal{R}_{1,\Psi(\mathcal{X})}$ on $\Omega \times \mathcal{I}$, we can project back on Ω the points $(\boldsymbol{x}, \psi(\boldsymbol{x})) \in \Omega \times \mathcal{I}$. In this way, we obtain a VSK interpolant $\mathcal{V}_\psi$ on Ω that is, using (5),

$$\mathcal{V}_\psi(\boldsymbol{x}) \coloneqq \sum_{k=1}^{N} c_k \Phi_\psi(\boldsymbol{x}, \boldsymbol{x}_k) = \sum_{k=1}^{N} c_k \Phi_1(\Psi(\boldsymbol{x}), \Psi(\boldsymbol{x}_k)) = \mathcal{R}_{1,\Psi(\mathcal{X})}(\Psi(\boldsymbol{x})). \tag{7}$$

The error and stability analysis of this varying scale process on Ω coincides with the analysis of a fixed scale kernel on $\Omega \times \mathcal{I}$. For further details and the analysis of the case with continuous scale functions, we refer the reader to [1]. We now briefly formalize the computational algorithm presented in [21] and we then investigate error bounds.

3 Variably scaled discontinuous kernels

We start by presenting the construction in the one dimensional case observing that the extension to the multidimensional case is almost straightforward (see below Subsection 3.2).

Let $\Omega = (a, b) \subset \mathbb{R}$ be an open interval and let $\xi \in \Omega$. We consider the discontinuous function $f : \Omega \longrightarrow \mathbb{R}$

$$f(x) \coloneqq \begin{cases} f_1(x), & a < x < \xi, \\ f_2(x), & \xi \leq x < b, \end{cases}$$

where f_1, f_2 are real valued smooth functions such that $\lim\limits_{x \to a^+} f_1(x)$ and $\lim\limits_{x \to b^-} f_2(x)$ exists finite and

$$f_2(\xi) \neq \lim_{x \to \xi} f_1(x)\,.$$

In this way, we have constructed a function f that has a jump discontinuity in $\xi \in \Omega$, being smooth elsewhere.

Our aim consists in approximating the function f on the set of nodes $\mathcal{X} \in \otimes$. Unfortunately the presence of jumps is the cause of oscillations of the recosrtructing process known as *Gibbs phenomenon*.

To approximate f on $\mathcal{X}$ we take interpolants of the form (7) with the main issue of considering discontinuous scale functions in the interpolation process.

Let $\alpha, \beta \in \mathbb{R},\ \alpha \neq \beta$ and $\mathcal{S} = \{\alpha, \beta\}$. We propose the following scale function $\psi : \Omega \longrightarrow \mathcal{S}$ defined as:

$$\psi(x) \coloneqq \begin{cases} \alpha, & x < \xi, \\ \beta, & x \geq \xi. \end{cases}$$

The function ψ is piecewise constant, having a jump discontinuity at ξ, as the function f. Let Φ_ε be a positive definite radial kernel on $\Omega \times \mathcal{S}$, possibly depending on a shape parameter $\varepsilon > 0$. We can consider a variably scaled kernel Φ_ψ on Ω as in (5).

More precisely, according to (3) we start by analysing the function φ_1 related to the kernel Φ_1 with fixed shape parameter $\varepsilon = 1$, that is

$$\varphi_1(\|\Psi(x) - \Psi(y)\|_2) = \varphi_1(\|(x, \psi(x)) - (y, \psi(y))\|_2) = \varphi_1(\sqrt{(x-y)^2 + (\psi(x) - \psi(y))^2}).$$

This implies

$$\varphi_1(\|\Psi(x) - \Psi(y)\|_2) = \begin{cases} \varphi_1(|x-y|), & x, y < \xi \quad \text{or} \quad x, y \geq \xi, \\ \varphi_1(\|(x, \alpha) - (y, \beta)\|_2), & x < \xi \leq y \quad \text{or} \quad y < \xi \leq x, \end{cases}$$

since $\varphi_1(\|(x, \alpha) - (y, \beta)\|_2) = \varphi_1(\|(x, \beta) - (y, \alpha)\|_2)$.

The so-constructed interpolant $\mathcal{V}_\psi : \Omega \longrightarrow \mathbb{R}$ on the set $\mathcal{X} = \{x_k,\ k = 1, \ldots, N\}$ is a discontinuous linear combination of functions $\Phi_\psi(\cdot, x_k)$ so defined:

- $a < x_k < \xi$

$$\Phi_\psi(x, x_k) = \begin{cases} \varphi_1(|x - x_k|), & x < \xi, \\ \varphi_1(\|(x, \alpha) - (x_k, \beta)\|_2), & x \geq \xi, \end{cases}$$

- $\xi \leq x_k < b$:

$$\Phi_\psi(x, x_k) = \begin{cases} \varphi_1(|x - x_k|), & x \geq \xi, \\ \varphi_1(\|(x, \alpha) - (x_k, \beta)\|_2), & x < \xi. \end{cases}$$

Therefore, the interpolant $\mathcal{V}_\psi$ is a linear combination of functions having a step discontinuity at ξ. See also [21]. We can easily generalize this procedure for a set of distinct discontinuity points on Ω; see the next section.

3.1 VSDKs: one dimensional case

To generalize the discussion carried out above, we first give the following definition.

Definition 3.1 *Let $\Omega = (a, b) \subset \mathbb{R}$ be an open interval, $\mathcal{S} = \{\alpha, \beta\}$ with $\alpha, \beta \in \mathbb{R}_{>0},\ \alpha \neq \beta$ and let $\mathcal{D} = \{\xi_j,\ j = 1, \ldots, \ell\} \subset \Omega$ be a set of distinct points such that $\xi_j < \xi_{j+1}$ for every j. Let $\psi : \Omega \longrightarrow \mathcal{S}$ be defined as*

$$\psi(x) \coloneqq \begin{cases} \alpha, & x \in (a, \xi_1) \text{ or } x \in [\xi_j, \xi_{j+1}), \quad \text{where } j \text{ is even}, \\ \beta, & x \in [\xi_j, \xi_{j+1}), \quad \text{where } j \text{ is odd}, \end{cases}$$

and

$$\psi(x)|_{[\xi_\ell, b)} \coloneqq \begin{cases} \alpha, & \ell \text{ is even}, \\ \beta, & \ell \text{ is odd}. \end{cases}$$

With this choice of the scale function ψ and referring to (5), we call the kernel Φ_ψ a VSDK on Ω.

Intuitively, if we deal with a function having jumps then we can approximate it with a linear combination of functions $\Phi_\psi(x, x_k)$ having jumps at the same locations.

For the analysis of the VSDKs introduced in Definition 3.1 we cannot rely on some important and well-known results of RBF interpolation. Therefore, before stating upper bounds for the VSDK interpolants in terms of the power function, we need some preliminary analysis.

Let Ω and $\mathcal{D}$ be as in Definition 3.1 and $n \in \mathbb{N}$. We define $\psi_n : \Omega \longrightarrow \mathcal{I} \subseteq (0, +\infty)$ as

$$\psi_n(x) \coloneqq \begin{cases} \alpha, & x \in (a, \xi_1 - 1/n) \text{ or } x \in [\xi_j + 1/n, \xi_{j+1} - 1/n) & j \text{ is even}, \\ \beta, & x \in [\xi_j + 1/n, \xi_{j+1} - 1/n) & j \text{ is odd}, \\ \gamma_1(x), & x \in [\xi_j - 1/n, \xi_j + 1/n) & j \text{ is odd}, \\ \gamma_2(x), & x \in [\xi_j - 1/n, \xi_j + 1/n) & j \text{ is even}, \end{cases} \tag{8}$$

$$\psi_n(x)|_{[\xi_\ell + 1/n, b)} \coloneqq \begin{cases} \alpha, & \ell \text{ is even}, \\ \beta, & \ell \text{ is odd}, \end{cases}$$

where γ_1, γ_2 are continuous, strictly monotonic functions such that:

$$\lim_{x \to \xi_{j+1} + 1/n} \gamma_1(x) = \gamma_2(\xi_j - 1/n) = \beta, \qquad \lim_{x \to \xi_{j+1} + 1/n} \gamma_2(x) = \gamma_1(\xi_j - 1/n) = \alpha.$$

From Definition 3.1, it is straightforward to verify that $\forall x \in \Omega$ the following pointwise convergence result holds

$$\lim_{n \to \infty} \psi_n(x) = \psi(x).$$

We point out that for every fixed $n \in \mathbb{N}$ the kernel Φ_{ψ_n} is a continuous VSK, hence it satisfies the error bound of Theorem 2.1. Moreover, for VSDKs we have the following results.

Theorem 3.1 *For every $x, y \in \Omega$, we have*

$$\lim_{n \to \infty} \Phi_{\psi_n}(x, y) = \Phi_\psi(x, y),$$

where Φ_ψ is the kernel considered in Definition 3.1.

Proof: Let us consider the map $\Psi_n(x) = (x, \psi_n(x))$ on Ω. We can write

$$\lim_{n \to \infty} \Phi_{\psi_n}(x, y) = \lim_{n \to \infty} \Phi_1(\Psi_n(x), \Psi_n(y)) = \lim_{n \to \infty} \varphi_1(\|\Psi_n(x) - \Psi_n(y)\|_2).$$

Recalling (3.1), we get

$$\begin{aligned} \lim_{n \to \infty} \varphi_1(\|\Psi_n(x) - \Psi_n(y)\|_2) &= \varphi_1\big(\lim_{n \to \infty} \|\Psi_n(x) - \Psi_n(y)\|_2\big) \\ &= \varphi_1\big(\sqrt{\lim_{n \to \infty} (x - y)^2 + (\psi_n(x) - \psi_n(y))^2}\big) \\ &= \varphi_1(\sqrt{(x - y)^2 + (\psi(x) - \psi(y))^2}) \\ &= \varphi_1(\|\Psi(x) - \Psi(y)\|_2) \\ &= \Phi_\psi(x, y). \end{aligned}$$

∎

Corollary 3.1 *Let $H_{\Phi_{\psi_n}}(\Omega) = span\{\Phi_{\psi_n}(\cdot, x),\ x \in \Omega\}$ be equipped with the bilinear form $(\cdot,\cdot)_{H_{\Phi_{\psi_n}}(\Omega)}$ and let $\mathcal{N}_{\Phi_{\psi_n}}(\Omega)$ be the related native space. Then, taking the limit of the basis functions, we obtain the space $H_{\Phi_\psi}(\Omega) = span\{\Phi_\psi(\cdot, x),\ x \in \Omega\}$ equipped with the bilinear form $(\cdot,\cdot)_{H_{\Phi_\psi}(\Omega)}$ and the related native space $\mathcal{N}_{\Phi_\psi}(\Omega)$.*

Proof: If $f \in H_{\Phi_\psi}(\Omega)$, then it can be expressed as a linear combination of basis functions $\Phi_\psi(\cdot, x),\ x \in \Omega$. From Theorem 3.1, we get that for every $x \in \Omega$

$$\lim_{n\to\infty} \Phi_{\psi_n}(\cdot, x) = \Phi_\psi(\cdot, x),$$

and so f is also linear combination of the functions $\lim_{n\to\infty} \Phi_{\psi_n}(\cdot, x),\ x \in \Omega$. This proves the thesis. ∎

We get an immediate consequence for the interpolant $\mathcal{V}_\psi$ too.

Corollary 3.2 *Let Ω, $\mathcal{S}$ and $\mathcal{D}$ be as in Definition 3.1. Let $f : \Omega \longrightarrow \mathbb{R}$ be a discontinuous function whose step discontinuities are located at the points belonging to $\mathcal{D}$. Moreover, let ψ_n and ψ be as in Theorem 3.1. Then, considering the interpolation problem with nodes $\mathcal{X} = \{x_k,\ k = 1, \dots, N\}$ on Ω, we have*

$$\lim_{n\to\infty} \mathcal{V}_{\psi_n}(x) = \mathcal{V}_\psi(x),$$

for every $x \in \Omega$.

Proof: Since $\mathcal{V}_\psi$ is a linear combination of the basis functions, the thesis follows from Theorem 3.1 and Corollary 3.1. ∎

To provide error bounds, we now only need to introduce the power function for a VSDK Φ_ψ on the set of nodes $\mathcal{X}$. From (4), we know that it is defined as

$$P_{\Phi_\psi,\mathcal{X}}(x) = \sqrt{\frac{\det(A_\psi(\mathcal{Y}))}{\det(A_\psi(\mathcal{X}))}}.$$

From Theorem 3.1 and Corollary 3.1, it easily follows that $\forall x \in \Omega$

$$P_{\Phi_\psi,\mathcal{X}}(x) = \lim_{n\to\infty} P_{\Phi_{\psi_n},\mathcal{X}}(x).$$

We are now able to state the following error bound for the interpolation via VSDKs.

Theorem 3.2 *Let Φ_ψ be a VSDK on $\Omega = (a, b) \subset \mathbb{R}$. Suppose that $\mathcal{X} = \{x_i, i = 1, \dots, N\} \subseteq \Omega$ have distinct points. For all $f \in \mathcal{N}_{\Phi_\psi}(\Omega)$ we have*

$$|f(x) - \mathcal{V}_\psi(x)| \leq P_{\Phi_\psi,\mathcal{X}}(x)\|f\|_{\mathcal{N}_{\Phi_\psi}(\Omega)}, \quad x \in \Omega.$$

Proof: For every $n \in \mathbb{N}$ and $x \in \Omega$, since the VSK Φ_{ψ_n} is continuous, we know that (see Theorem 2.1)

$$|f(x) - \mathcal{V}_{\psi_n}(x)| \leq P_{\Phi_{\psi_n},\mathcal{X}}(x)\|f\|_{\mathcal{N}_{\Phi_{\psi_n}}(\Omega)}.$$

Considering the limit as $n \to \infty$ in the previous inequality and recalling all the results of this subsection, the thesis follows. ∎

Theorem 3.2, as the classical bound for the RBF interpolants, limits the error in terms of the power function and consequently takes into account both the kernel and data. Similar results also hold for the multidimensional case, as shown in the next subsection.

3.2 VSDKs: multidimensional case

VSDKs rely upon the classical RBF bases and therefore in principle they are suitable to be implemented in any dimension. However, since the geometry now is more complex than in 1D, we need to carefully define the scale function ψ.

Let $\Omega \subset \mathbb{R}^d$ be an open subset with Lipschitz boundary. In our discussion, we consider step discontinuous functions $f : \Omega \longrightarrow \mathbb{R}$ such that there exists a disjoint partition $\mathcal{P} = \{R_1, \ldots, R_m\}$ of regions having Lipschitz boundaries. That is all the jumps of f lye along $(d-1)$-dimensional manifolds $\gamma_1, \ldots, \gamma_p$ which verify

$$\gamma_i \subseteq \bigcup_{i=1}^{m} \partial R_i \setminus \partial\Omega, \quad \forall i = 1, \ldots, p.$$

Then, a suitable scale function ψ for interpolating f via VSDKs can be defined as follows.

Definition 3.2 *Let $\Omega \subset \mathbb{R}^d$ be an open subset with Lipschitz boundary, $\mathcal{S} = \{\alpha_1, \ldots, \alpha_m\}$ real distinct values and $\mathcal{P} = \{R_1, \ldots, R_m\}$ a partition of Ω whose elements are regions having Lipschitz boundaries. Define $\psi : \Omega \longrightarrow \mathcal{S}$ as*

$$\psi(\boldsymbol{x})|_{R_i} \coloneqq \alpha_i.$$

With this choice of the scale function ψ and referring to (5), we call the kernel Φ_ψ a VSDK on Ω.

Remark 3.1 *In Definition 3.2 we choose a scale function which emulates the properties of the one-dimensional function of Definition 3.1. The difference is that the multidimensional ψ could be discontinuous not just at the same points as f, but also on other nodes. Precisely, if we are able to choose $\mathcal{P}$ so that*

$$\bigcup_{i=1}^{p} \gamma_i = \bigcup_{i=1}^{m} \partial R_i \setminus \partial\Omega,$$

then f and ψ have the same discontinuities. Otherwise, if

$$\bigcup_{i=1}^{p} \gamma_i \subset \bigcup_{i=1}^{m} \partial R_i \setminus \partial\Omega,$$

then ψ is discontinuous along $\bigcup_{i=1}^{m} \partial R_i \setminus \left(\partial\Omega \cup \bigcup_{i=1}^{p} \gamma_i\right)$, while f is not.

Since our aim is to use ψ to represent f in a proper way near the discontinuities, this would not be a problem, as we will see later in the numerical examples.

The theoretical analysis in the multidimensional case covers the same path of the one-dimensional setting. Indeed, we consider continuous scale functions $\psi_n : \Omega \longrightarrow \mathcal{I} \subseteq (0, +\infty)$ such that $\forall \boldsymbol{x} \in \Omega$,

$$\lim_{n\to\infty} \psi_n(\boldsymbol{x}) = \psi(\boldsymbol{x}),$$

and

$$\lim_{n\to\infty} \mathcal{V}_{\psi_n}(\boldsymbol{x}) = \mathcal{V}_\psi(\boldsymbol{x}),$$

for every $\boldsymbol{x} \in \Omega$.

We omit this easy extension of all considerations and results of Subsection 3.1 and we state the following error bound.

Theorem 3.3 *Let Φ_ψ be a VSDK as in Definition 3.2. Suppose that $\mathcal{X} = \{\boldsymbol{x}_i, i = 1, \dots, N\} \subseteq \Omega$ have distinct points. For all $f \in \mathcal{N}_{\Phi_\psi}(\Omega)$ we have*

$$|f(\boldsymbol{x}) - \mathcal{V}_\psi(\boldsymbol{x})| \leq P_{\Phi_\psi,\mathcal{X}}(\boldsymbol{x}) \|f\|_{\mathcal{N}_{\Phi_\psi}(\Omega)}, \quad \boldsymbol{x} \in \Omega.$$

Proof: We refer to Theorem 3.2 and to the considerations made in this section. ∎

The error analysis for VSDKs shows strong similarities with the standard RBF reconstruction. However, the discontinuity introduced on the scale functions and consequently on kernels, as evident from the experiments that follow, enables us to intervene on the Gibbs phenomenon.

4 Numerics

The numerical experiments that follow have been carried out with MATLAB on an Intel(R) Core(TM) i5-4200U CPU @ 2.30 GHz processor. We remark that the software for VSDK interpolation can be downloaded at the link reported in the introduction.

We consider three strictly positive definite RBFs having different regularities

$$\begin{array}{ll} \varphi_\varepsilon^1(r) = e^{-\varepsilon r}, & \textit{Matern } C^0, \\ \varphi_\varepsilon^2(r) = e^{-\varepsilon r}\left(15 + 15\varepsilon r + 6\varepsilon^2 r^2 + \varepsilon^2 r^3\right), & \textit{Matern } C^6, \\ \varphi_\varepsilon^3(r) = e^{-\varepsilon^2 r^2}, & \textit{Gaussian } C^\infty. \end{array} \tag{9}$$

To point out the accuracy of our tests, both in 1D and 2D cases, we refer to the Maximum Absolute Error (MAE) and the Root Mean Square Error (RMSE). Once the interpolant is constructed, we evaluate it on a grid of S evaluation points $\{\boldsymbol{z}_1, \dots, \boldsymbol{z}_S\}$ so that

$$\text{MAE} = \max_{1 \leq i \leq Z} |f(\boldsymbol{z}_i) - \mathcal{V}_\psi(\boldsymbol{z}_i)|, \qquad \text{RMSE} = \sqrt{\frac{1}{Z}\sum_{i=1}^{Z} \left(f(\boldsymbol{z}_i) - \mathcal{V}_\psi(\boldsymbol{z}_i)\right)^2}.$$

Further, we also estimate the upper bound for the error by computing the Maximum of the Power Function (MPF)

$$\text{MPF} = \max_{1 \leq i \leq Z} P_{\Phi_\psi,\mathcal{X}}(\boldsymbol{z}_i).$$

In the 2D case we also deal with grey-scale images and thus we consider the Structural Similarity Index (SSIM), which is a well-known parameter that indicates the similarity between two images. The SSIM index lies in the interval $[0, 1]$ (the value 1 corresponds to identical images).

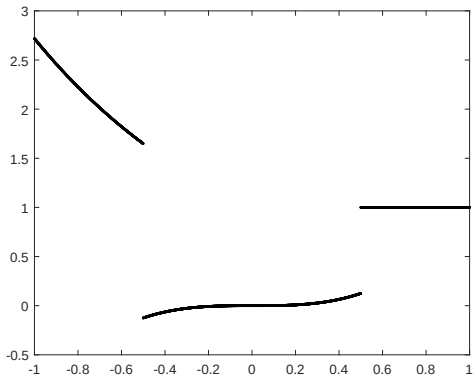

(a) The function f_1.

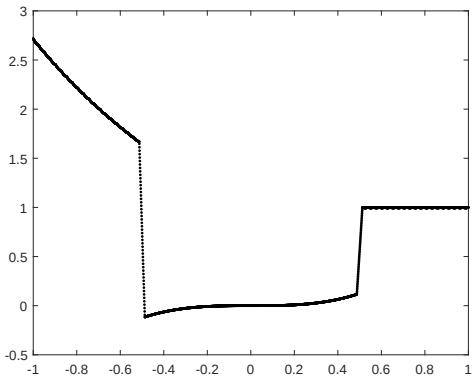

(b) The interpolant obtained using φ_ε^1.

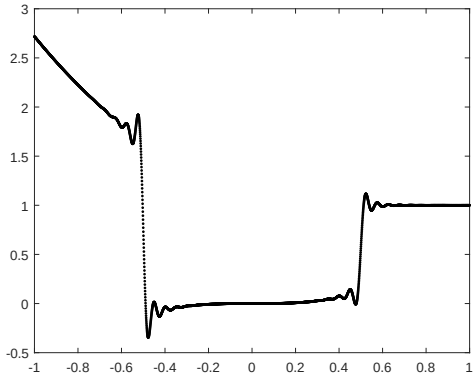

(c) The interpolant obtained using φ_ε^2.

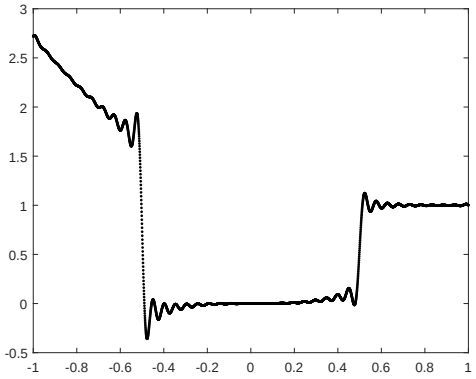

(d) The interpolant obtained using φ_ε^3.

Figure 1: The function f_1 and the classical interpolants on $\mathcal{X}$ obtained using different kernel functions.

4.1 A toy example

Let $\Omega = (-1, 1)$,

$$f_1(x) = \begin{cases} e^{-x}, & -1 < x < -0.5, \\ x^3, & -0.5 \leq x < 0.5, \\ 1, & 0.5 \leq x < 1. \end{cases}$$

and

$$\mathcal{X} = \left\{ x_j = -1 + \frac{(j-1)}{39},\ j = 1, \ldots, 79 \right\}.$$

We evaluate then the interpolant on a grid of equispaced points on Ω with step size 5.00E$-$4.

First, as described in (2), we interpolate the function f_1 via classical RBF interpolation on $\mathcal{X}$, using the kernel functions reported in (9). For such RBFs we select the optimal shape parameter $\varepsilon*$ via Leave One Out Cross Validation (LOOCV) ([12] for a general overview or to [6] for particular instances on the topic). The resulting interpolants are plotted in Figure 1.

In Table 1 we report the values of MAE and RMSE with respect to f_1 and the maximum values of the power function evaluated at the same set of nodes. The errors are similar expect

Table 1: Results of classical RBF reconstruction for f_1.

RBFs	φ_ε^1	φ_ε^2	φ_ε^3
MAE	$8.98\text{E}-01$	$8.96\text{E}-01$	$8.96\text{E}-01$
RMSE	$6.49\text{E}-02$	$6.94\text{E}-02$	$7.25\text{E}-02$
MPF	$3.14\text{E}-01$	$1.15\text{E}-01$	$2.01\text{E}-02$

Table 2: Results of VSK and VSDK reconstruction for f_1 using φ_1^1.

Scale functions	ψ_{10}	ψ_{50}	ψ_{500}	ψ
MAE	$9.03\text{E}-01$	$9.59\text{E}-01$	$1.05\text{E}+00$	$2.97\text{E}-02$
RMSE	$6.47\text{E}-02$	$6.47\text{E}-02$	$2.70\text{E}-02$	$1.43\text{E}-03$
MPF	$2.55\text{E}-01$	$5.53\text{E}-01$	$6.56\text{E}-01$	$1.59\text{E}-01$

for φ_ε^1 that guarantees better results. Indeed, as expected, the corresponding reconstruction is less affected by the Gibbs phenomenon, due to the poor regularity of φ_ε^1.

Concerning our approach: the function f_1 presents two points of discontinuity $\xi_1 = -0.5$ and $\xi_2 = 0.5$. Taking into account (8), we define the scale function for VSKs for f_1,

$$\psi_n(x) \coloneqq \begin{cases} 1, & x \in (-1, \xi_1 - 1/n) \text{ or } x \in [\xi_2 + 1/n, 1), \\ 2, & x \in [\xi_1 + 1/n, \xi_2 - 1/n), \\ (nx - \xi_1 n + 3)/2, & x \in [\xi_1 - 1/n, \xi_1 + 1/n), \\ (-nx + \xi_2 n + 3)/2, & x \in [\xi_2 - 1/n, \xi_2 + 1/n). \end{cases} \tag{10}$$

Moreover, considering the pointwise limit as $n \to \infty$ of $\psi_n(x)$ we consider for VSDKs the discontinuous scale function:

$$\psi(x) = \begin{cases} 1, & x \in (-1, \xi_1) \text{ or } x \in [\xi_2, 1), \\ 2, & x \in [\xi_1, \xi_2). \end{cases} \tag{11}$$

Finally, for each of the RBFs considered in (9) we first take the scale function ψ_n and compute the VSK interpolation of f_1 by considering increasing values of n ($n = 10, 50, 500$). Then we approximate f_1 using the VSDK determined by ψ (see formulae (10) and (11)). The graphical results for the three variably scaled (discontinuous) kernels are reported in Figures 2–4, while the accuracy indicators are shown in Tables 2–4.

From the figures, we can graphically note how the reconstruction via VSDKs is indeed the limit of the continuous case. As expected the C^0 RBF combined with the VSKs does not show a huge Gibbs phenomenon. Using the other kernels, we note that such oscillations are progressively reduced as n increases and graphically disappear when using VSDKs.

From the results reported in this subsection it is evident that the maximum value of the power function decreases as n increases. The fact that the power function for VSDKs assumes smaller values than thos of VSKs is confirmed only by numerical evidence. Indeed, in some cases the maximum value attained by the power function is sensibly higher for VSDKs, even compared to the classical RBF reconstruction.

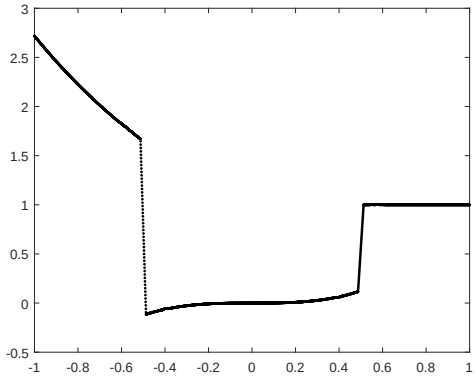

(a) The VSK interpolant using ψ_{10}.

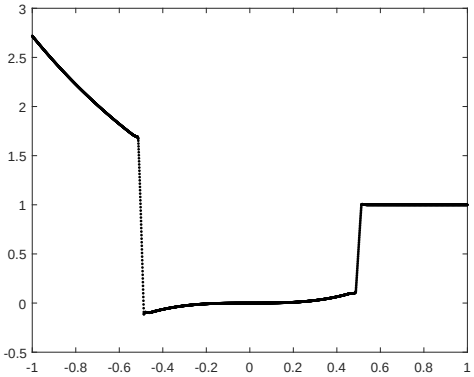

(b) The VSK interpolant using ψ_{50}.

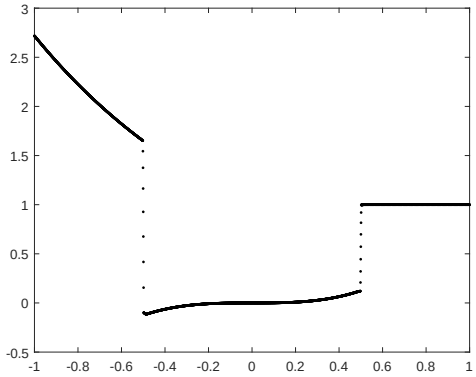

(c) The VSK interpolant using ψ_{500}.

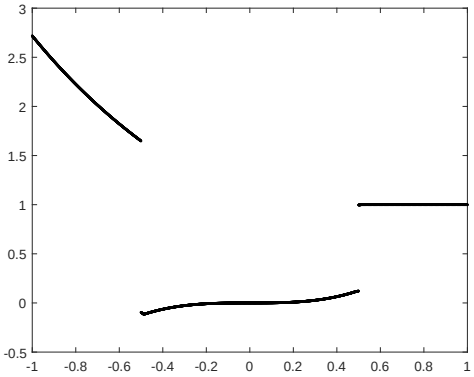

(d) The VSDK interpolant using ψ.

Figure 2: VSK and VSDK reconstructions of f_1 on $\mathcal{X}$ using φ_1^1.

Table 3: Results of VSK and VSDK reconstruction for f_1 using φ_1^2.

Scale functions	ψ_{10}	ψ_{50}	ψ_{500}	ψ
MAE	$8.96\text{E}-01$	$8.92\text{E}-01$	$8.89\text{E}-01$	$6.08\text{E}-06$
RMSE	$6.96\text{E}-02$	$5.86\text{E}-02$	$2.60\text{E}-02$	$3.34\text{E}-07$
MPF	$5.11\text{E}-02$	$6.40\text{E}-02$	$1.79\text{E}-01$	$5.70\text{E}-02$

Table 4: Results of VSK and VSDK reconstruction for f_1 using φ_3^1.

Scale functions	ψ_{10}	ψ_{50}	ψ_{500}	ψ
MAE	$8.96\text{E}-01$	$8.86\text{E}-01$	$9.92\text{E}-01$	$1.19\text{E}-04$
RMSE	$9.78\text{E}-02$	$5.84\text{E}-02$	$2.51\text{E}-02$	$3.50\text{E}-05$
MPF	$1.21\text{E}-02$	$2.07\text{E}-02$	$3.36\text{E}-01$	$1.96\text{E}-02$

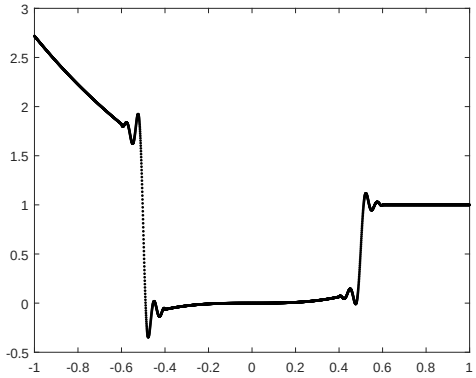

(a) The VSK interpolant using ψ_{10}.

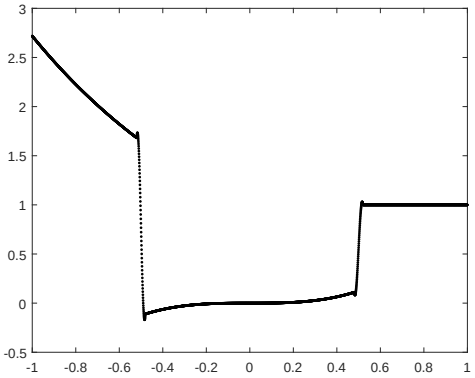

(b) The VSK interpolant using ψ_{50}.

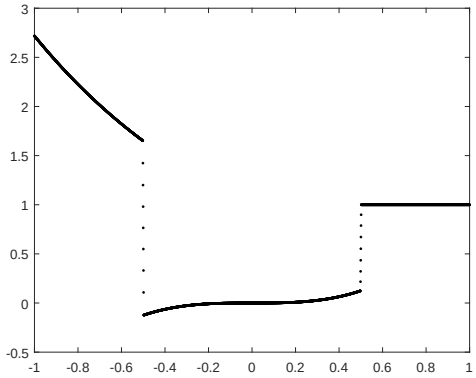

(c) The VSK interpolant using ψ_{500}.

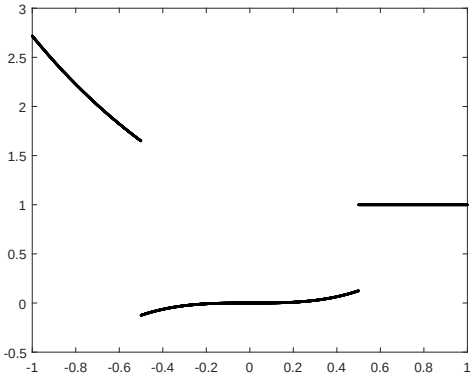

(d) The VSDK interpolant using ψ.

Figure 3: VSK and VSDK reconstructions of f_1 on $\mathcal{X}$ using φ_1^2.

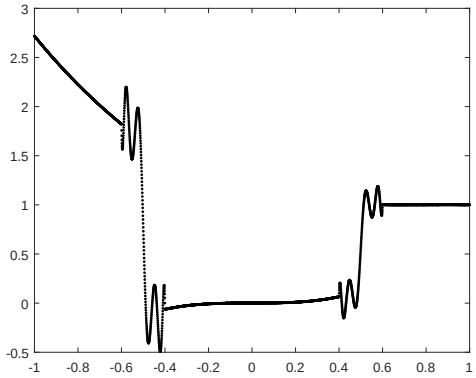

(a) The VSK interpolant using ψ_{10}.

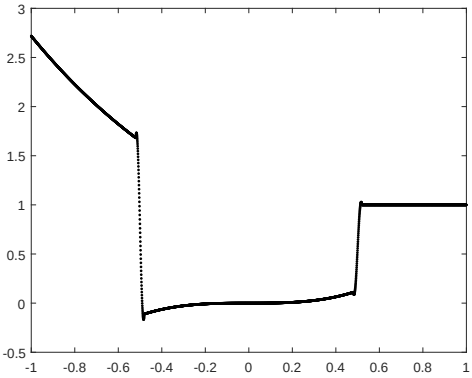

(b) The VSK interpolant using ψ_{50}.

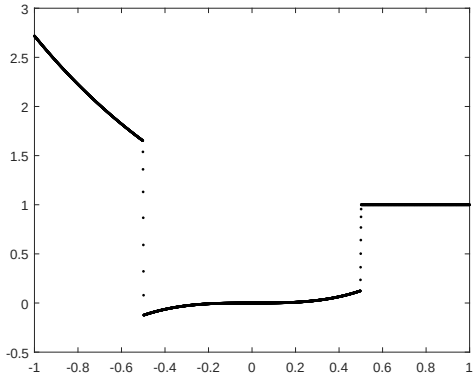

(c) The VSK interpolant using ψ_{500}.

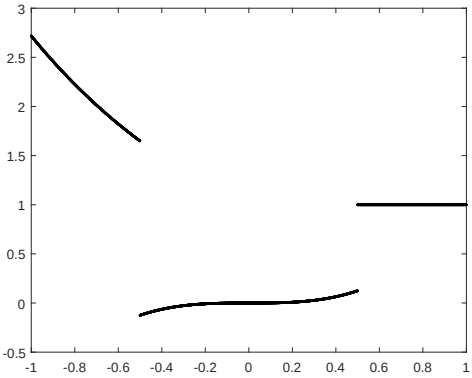

(d) The VSDK interpolant using ψ.

Figure 4: VSK and VSDK reconstructions of f_1 on $\mathcal{X}$ using φ_1^3.

Table 5: Results of classical RBF reconstruction for f_2.

RBFs	φ_ε^1	φ_ε^2	φ_ε^3
MAE	$1.30\text{E}-00$	$1.72\text{E}-00$	$1.75\text{E}-00$
RMSE	$9.80\text{E}-02$	$1.21\text{E}-01$	$1.53\text{E}-01$
MPF	$1.03\text{E}-02$	$1.11\text{E}-00$	$9.85\text{E}-01$
SSIM	0.908	0.776	0.541

4.2 Tests with artificial data

Let $\Omega = (-1, 1)^2$. We consider two test functions,

$$f_2(x,y) = \begin{cases} e^{-(x^2+y^2)}, & x^2+y^2 \leq 0.6, \\ x+y, & x^2+y^2 > 0.6, \end{cases}$$

$$f_3(x,y) = \begin{cases} 2(1-e^{-(y+0.5)^2}), & |x| \leq 0.5,\ |y| \leq 0.5, \\ 4(x+0.8), & -0.8 \leq x \leq -0.65,\ |y| \leq 0.8, \\ 0.5, & 0.65 \leq x \leq 0.8,\ |y| \leq 0.2, \\ 0, & \textit{otherwise.} \end{cases}$$

We take 1089 Halton points on Ω as interpolation nodes and we evaluate the approximant on equispaced points on Ω with step size $1.00\text{E}-2$.

Similarly to the one-dimensional case in Section 4.1, we interpolate the functions f_2 and f_3 via classical RBF interpolation on the set of nodes $\mathcal{X}$, using the kernel functions in (9) and selecting the optimal shape parameter ε via LOOCV. Finally, we apply VSDKs and we evaluate the final results.

We start our discussion from the function f_2. The resulting standard RBF interpolants for f_2 are plotted in Figure 5. As expected, the infinitely smooth Gaussian RBF introduces huge oscillations, while with functions with low regularity, the Gibbs phenomenon is less evident.

In Table 5 we report the accuracy indicators. We can observe that φ_ε^1 outperforms the other two kernels in terms of SSIM index. Indeed, the related reconstruction is less affected by the Gibbs phenomenon, as graphically visible.

In order to perform a VSDK reconstruction of f_2, we need a suitable scale function satisfying the Definition 3.2. For this purpose, we consider the function ψ^2 defined as

$$\psi^2(x,y) = \begin{cases} 1, & x^2+y^2 \leq 0.6, \\ 2, & x^2+y^2 > 0.6. \end{cases} \tag{12}$$

We show the final reconstructions using VSDKs with different kernels in Figure 6, while in Table 6 we report the values of the considered errors and parameters. We recover also for the 2D case the pattern already discovered about the fact that VSDKs reconstruct the jumps without graphically introducing oscillations, also with C^∞ RBFs.

Considering now the function f_3, we show in Figure 7 and in Table 7 the results obtained via classic RBF reconstructions.

We can observe a behavior that is similar to what we obtained for f_2. Passing to VSDKs

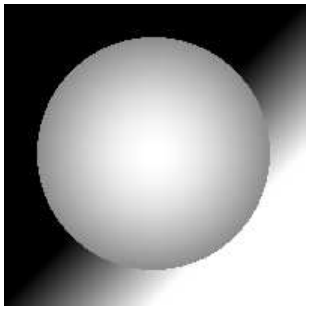

(a) The function f_2.

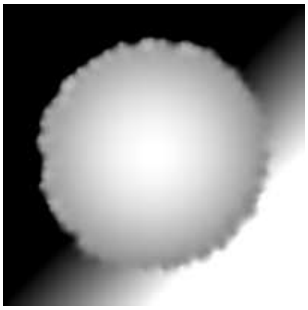

(b) The interpolant obtained using φ_ε^1.

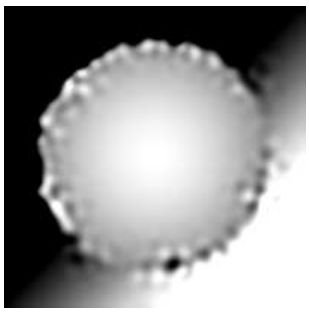

(c) The interpolant obtained using φ_ε^2.

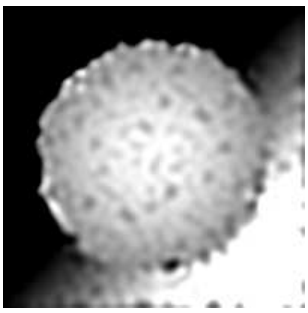

(d) The interpolant obtained using φ_ε^3.

Figure 5: The function f_2 and the classical RBF interpolants on $\mathcal{X}$ obtained using different kernel functions.

Table 6: Results of VSDK reconstructions for f_2.

RBFs	φ_1^1	φ_1^2	φ_1^3
MAE	$1.82\text{E}-01$	$8.20\text{E}-05$	$1.03\text{E}-05$
RMSE	$5.29\text{E}-03$	$1.13\text{E}-06$	$5.70\text{E}-07$
MPF	$3.52\text{E}-01$	$1.43\text{E}-02$	$3.65\text{E}-04$
SSIM	0.997	0.999	0.999

Table 7: Results of classical RBF reconstruction for f_3.

RBFs	φ_ε^1	φ_ε^2	φ_ε^3
MAE	$1.23\text{E}-00$	$1.56\text{E}-00$	$1.74\text{E}-00$
RMSE	$8.60\text{E}-02$	$9.89\text{E}-02$	$1.09\text{E}-01$
MPF	$9.48\text{E}-01$	$3.80\text{E}-00$	$9.94\text{E}-01$
SSIM	0.843	0.788	0.751

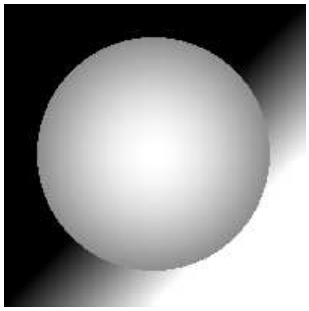

(a) VSDK reconstruction using φ_1^1.

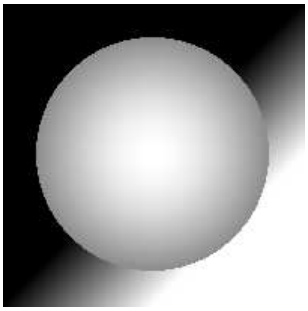

(b) VSDK reconstruction using φ_1^2.

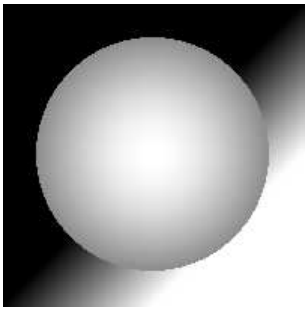

(c) VSDK reconstruction using φ_1^3.

Figure 6: VSDK reconstructions of f_2 on $\mathcal{X}$ using the scale function ψ^2.

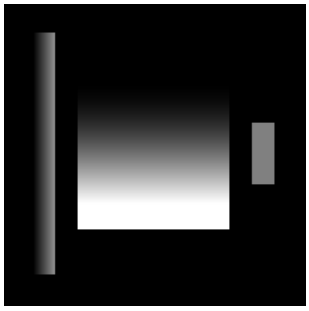

(a) The function f_3.

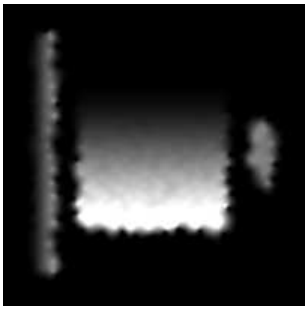

(b) The interpolant obtained using φ_ε^1.

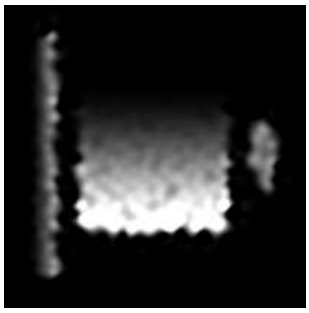

(c) The interpolant obtained using φ_ε^2.

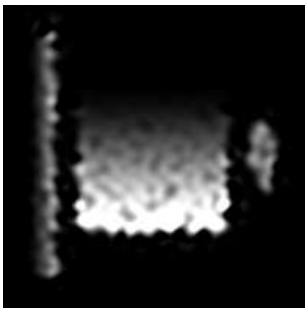

(d) The interpolant obtained using φ_ε^3.

Figure 7: The function f_3 and the classical interpolants on $\mathcal{X}$ obtained using different kernel functions.

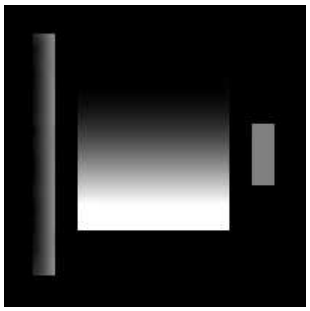

(a) VSDK reconstruction using φ_1^1.

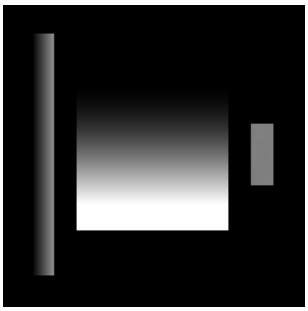

(b) VSDK reconstruction using φ_1^2.

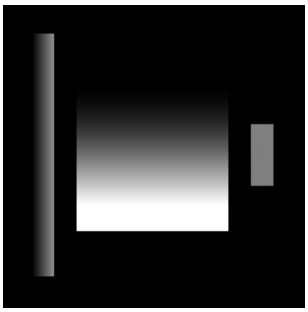

(c) VSDK reconstruction using φ_1^3.

Figure 8: VSDK reconstructions of f_3 on $\mathcal{X}$ using the scale function ψ^3.

for f_3, we consider the scale function ψ^3 defined as

$$\psi^3(x,y) = \begin{cases} 1, & |x| \leq 0.5,\ |y| \leq 0.5, \\ 2, & -0.8 \leq x \leq -0.65,\ |y| \leq 0.8, \\ 3, & 0.65 \leq x \leq 0.8,\ |y| \leq 0.2, \\ 0, & \textit{otherwise.} \end{cases} \tag{13}$$

We point out that the set of discontinuity points of f_3 is strictly contained in the set of discontinuity points of ψ^3, which is a situation considered in the Remark 3.1. We presents the final results in Figure 8 and in Table 8.

We can observe that the VSDK reconstructions using φ_1^2 and φ_1^3 are not affected by the Gibbs phenomenon as in the classical RBF reconstructions and they outperform the reconstruction obtained using φ_1^1. The same holds for f_3.

Furthermore, for both the test functions considered in this section, the SSIM with VSDKs is about 1, which means that graphically there is a high similarity between the original and reconstructed image.

Concerning the maximum value of the power function for VSDKs, we can note that for both f_2 and f_3 it is comparable to the one obtained via standard RBFs. However, the reader

Table 8: Results of VSDK reconstructions for f_3.

RBFs	φ_1^1	φ_1^2	φ_1^3
MAE	$1.68\text{E}-01$	$5.71\text{E}-04$	$1.71\text{E}-05$
RMSE	$6.75\text{E}-03$	$9.89\text{E}-06$	$4.84\text{E}-07$
MPF	$3.52\text{E}-01$	$2.39\text{E}-02$	$1.40\text{E}-03$
SSIM	0.993	0.999	0.999

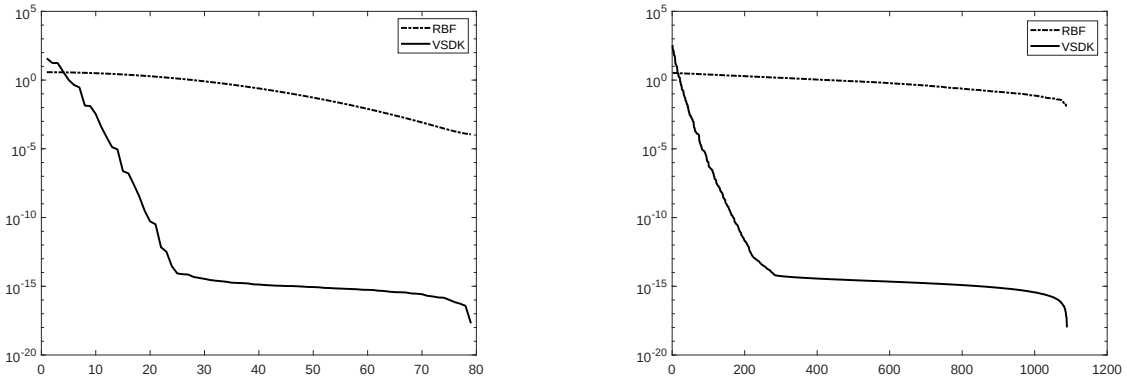

(a) Singular values in 1D.

(b) Singular values in 2D.

Figure 9: Singular values of the interpolation matrices for RBF and VSDK reconstruction.

should note that usually it reaches lower values than the ones achieved via the classical schemes. This reflects directly on the error (as theoretically proved in Theorem 3.3).

In general, for both 1D and 2D, the most promising results are the ones obtained via VSDKs and the Gaussian function. Indeed, it is well known that C^∞ functions introduce Gibbs phenomenon. To have a better understanding of the reason why VSDKs outperform the classical RBF reconstruction when using the Gaussian, we plot the decay of the singular values of the kernel matrix in Figure 9. In the left frame we plot the singular values for the equispaced data considered for the 1D, while, in the right frame we consider the 2D Halton data used in this subsection and the scale function ψ^2. We can note that the VSDKs act somehow as filters, indeed the decay of the singular values is very fast compared to the standard RBF reconstruction. In this sense, VSDKs could potentially be used together with compression techniques, such as principal component analysis, leading to reduced models and maintaining a good accuracy. Further investigations in this direction are needed.

5 Application to satellite images

The modeling and analysis of data, for instance, coming from distributed measurements of physical quantities and satellite images is a challenging computational issue. Because of the huge size that some of these data sets achieve, reduced models such as the one presented in [19] are strongly advised. Nevertheless, the Gibbs phenomenon might affect also in this case the accuracy of the approximation. Thus, in this example, we show how VSDKs can

Figure 10: Example of satellite image measuring the soil moisture.

intervene in this direction, sensibly reducing the oscillations.

We consider the satellite image reported in Figure 10, taken by SMAP satellite on April 2015 and measuring the soil moisture over the world. It is composed by a grid of 3856×1624 pixels. For dealing with the whole image, one needs to use reduced models, such as the one investigated in [20]. Moreover, if one only concentrates on a small portion of the image, e.g. on Portugal, the high resolution is lost (trivially due to zooming). In this case, a reconstruction scheme is necessary.

Focusing on Portugal, we obtain an image composed by $N = 82 \times 39 = 3198$ pixels. After using these data to reconstruct the image, we evaluate it on a finer grid of evaluation points, composed by $Z = 244 \times 155 = 28060$ pixels. Such a computation can be seen as a standard zoom, which might introduce Gibbs oscillations. They are indeed visible if, for instance, we reconstruct the image with the Wendland's C^2 RBF defined by:

$$\varphi_\varepsilon^4(r) = (1 - \varepsilon r)_+^4(4\varepsilon r + 1), \quad \text{Wendland } C^2,$$

where $(\cdot)_+$ denotes the truncated power function. We consider the Wendland's compactly supported C^2 RBF because it is well-known that by properly scaling the support of the basis function, it might lead to sparse interpolation systems and thus gaining in terms of stability, reducing the usual high condition number of the interpolation matrix. Despite this ability, the reconstruction via the classical method still suffers from the Gibbs phenomenon, see Figure 11 (left). Such oscillations are removed by VSDKs; refer to Figure 11 (right). This example with real data is also devoted to show that VSDKs perform well also when the discontinuity is analytically unknown. In this case the curve defining the discontinuity lies along the coast of Portugal and it has been approximated by means of Sobel detection scheme; see e.g. [25].

6 Conclusions

In this paper we have presented a robust method for sensibly reducing non-physical oscillations due to the Gibbs phenomenon. The accuracy of the proposed method has been

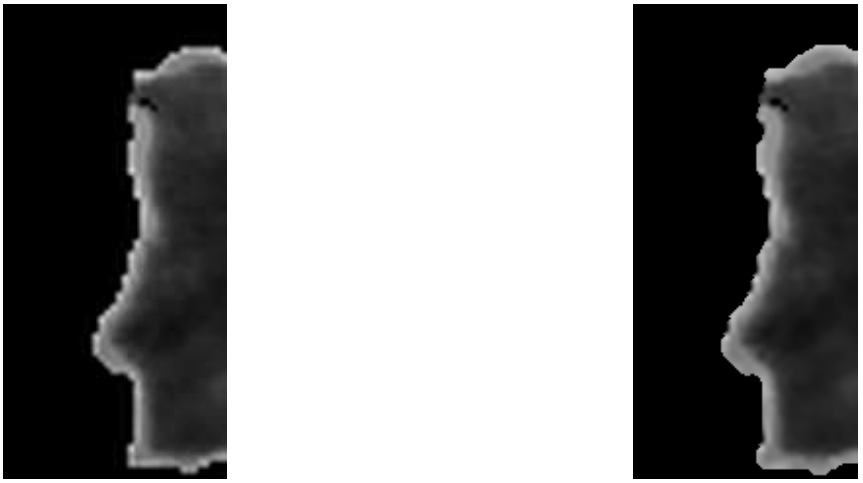

(a) RBF (b) VSDK

Figure 11: The approximation of soil moisture over Portugal via classical RBF reconstruction (left) and VSDKs (right).

studied theoretically and many numerical experiments confirm its effectiveness. Indeed, the reconstruction via VSDKs outperforms the standard one when jumps occur.

Work in progress consists in further investigations about the detection of discontinuities when dealing with real data. Moreover, the current study might be useful for the problem of image reconstruction in the context of magnetic particle imaging [8]. Future work in this direction is also needed. Finally, for smooth RBFs, we should study the behaviour of VSDKs when rational interpolants are used [9, 17].

Acknowledgments

This research has been accomplished within Rete ITaliana di Approssimazione (RITA), partially supported by GNCS-INδAM and UE ERA-PLANET GA n. 689443.

References

[1] M. Bozzini, L. Lenarduzzi, M. Rossini, R. Schaback, *Interpolation with variably scaled kernels*, IMA J. Numer. Anal. **35** (2015), pp. 199–219.

[2] J.F. Canny, *A computational approach to edge detection*, IEEE TPAMI, **8** (1986), pp. 34–43.

[3] F. Carnevali, *Interpolazione con basi radiali a scala variabile*, master thesis, University of Milano Bicocca, 2014.

[4] R. Cavoretto, A. De Rossi, *A trivariate interpolation algorithm using a cube-partition searching procedure*, SIAM J. Sci. Comput. **37** (2015), pp. A1891–A1908.

[5] R. Cavoretto, S. De Marchi, A. De Rossi, E. Perracchione, G. Santin, *Partition of unity interpolation using stable kernel-based techniques*, Appl. Numer. Math. **116** (2017), pp. 95–107.

[6] R. Cavoretto, A. De Rossi, E. Perracchione, *Optimal selection of local approximants in RBF-PU interpolation*, to appear on J. Sci. Comput. (2017).

[7] S. De Marchi, *On optimal center locations for radial basis function interpolation: computational aspects*, Rend. Sem. Mat. Univ. Pol. Torino **61** (2003), pp. 343–358.

[8] S. De Marchi, W. Erb, F. Marchetti, *Spectral filtering for the reduction of the Gibbs phenomenon for polynomial approximation methods on Lissajous curves with applications in MPI*, Dolomites Res. Notes Approx. **10** (2017), pp. 128–137.

[9] S. De Marchi, A. Martínez, E. Perracchione, *Fast and stable rational RBF-based partition of unity interpolation*, to appear on J. Comput. Appl. Math. 2018.

[10] S. De Marchi, G. Santin, *Fast computation of orthonormal basis for RBF spaces through Krylov space methods*, BIT **55** (2015), pp. 949–966.

[11] S. De Marchi, R. Schaback, H. Wendland, *Near-optimal data-independent point locations for radial basis function interpolation*, Adv. Comput. Math. **23** (2005), pp. 317–330.

[12] G.E. Fasshauer, M.J. McCourt, *Kernel-based Approximation Methods Using* Matlab, World Scientific, Singapore, 2015.

[13] G.E. Fasshauer, *Meshfree Approximations Methods with* Matlab, World Scientific, Singapore, 2007.

[14] B. Fornberg, N. Flyer, *The Gibbs Phenomenon in Various Representations and Applications*, chapter The Gibbs phenomenon for radial basis functions. Sampling Publishing, Potsdam, NY, 2008.

[15] B. Fornberg, E. Larsson, N. Flyer, *Stable computations with Gaussian radial basis functions*, SIAM J. Sci. Comput. **33** (2011), pp. 869–892.

[16] D. Gottlieb, C.W. Shu, *On the Gibbs phenomenon and its resolution*, SIAM Review **39** (1997), pp. 644–668.

[17] S. Jakobsson, B. Andersson, F. Edelvik, *Rational radial basis function interpolation with applications to antenna design*, J. Comput. Appl. Math. **233** (2009), pp. 889–904.

[18] J.H. Jung, *A note on the Gibbs phenomenon with multiquadric radial basis functions*, Appl. Num. Math. **57** (2007), pp. 213–219.

[19] E. Perracchione, M. Polato, D. Tran, F. Piazzon, F. Aiolli, S. De Marchi, S. Kollet, C. Montzka, A. Sperduti, M. Vianello, M. Putti, *Modelling and processing services and tools*, 2018, GEO Essential Deliverable 1.3.

[20] F. Piazzon, A. Sommariva, M. Vianello, *Caratheodory-Tchakaloff Least Squares*, Sampling Theory and Applications 2017, IEEE Xplore Digital Library, 12017.

[21] L. Romani, M. Rossini, D. Schenone, *Edge detection methods based on RBF interpolation*, to appear on J. Comput. Appl. Math. 2018.

[22] M. Rossini, *Interpolating functions with gradient discontinuities via variably scaled kernels*, Dolom. Res. Notes Approx. **11** (2018), pp. 3–14.

[23] S.A. Sarra, *Digital total variation filtering as postprocessing for radial basis function approximation methods*, Comput. Math. Appl. **52** (2006), pp. 1119–1130.

[24] S.A. Sarra, E.J. Kansa, *Multiquadric radial basis function approximation methods for the numerical solution of partial differential equations*, Tech Science Press, 2010.

[25] M. Sharifi, M. Fathy, M.T. Mahmoudi, *A Classified and Comparative Study of Edge Detection Algorithms*, in Proc. Int. Conf. on Inform. Technology: Coding and Computing, Las Vegas, USA, 2002, pp. 117–120.

[26] H. Wendland, *Scattered Data Approximation*, Cambridge Monogr. Appl. Comput. Math., vol. 17, Cambridge Univ. Press, Cambridge, 2005.